Department of Physics and Astronomy
University of Heidelberg

Bachelor Thesis in Physics
submitted by

Christin Proß

born in Geislingen an der Steige (Germany)

2016

Analysis of Fetch Dependency of the Slope of Wind-Water Waves

This Bachelor Thesis has been carried out by Christin Proß at the
Institute of Environmental Physics in Heidelberg
under the supervision of
Prof. Bernd Jähne

Abstract:

In this thesis mean square slope has been calculated from slope images which were recorded by the Imaging Slope Gauge (ISG) at the annular wind-wave tank Aeolotron in Heidelberg. The calculations have been realized using three different methods, which are, (i) calculation of the variance, (ii) integration of the slope power spectrum and (iii) fitting the probability distribution function of slope with a model function. The resulting values have been compared to each other and to the existing live evaluation of the ISG for a wide range of wind and fetch conditions. Also the fetch dependence of mean square slope has been analyzed, which obtains information about the evolution of a wave field.

Additionally the slope images have been separated with the use of band pass filters into slope images of gravity waves and capillary waves. By separating gravity from capillary waves it was possible to analyze their slope probability distribution functions individually.

Übersicht:

Im Rahmen dieser Arbeit wurde die mittlere quadratische Neigung aus Neigungsbilder berechnet, welche mit der Imaging Slope Gauge (ISG) am Aeolotron, einem ringförmigen Wind-Wellen Kanal in Heidelberg aufgenommen wurden. Zur Berechnung wurden drei verschiedene Methoden angewandt, (i) Berechnen der Varianz, (ii) Integration des Neigungsspektrums und (iii) Anfitten einer Modellfunktion an die Häufigkeitsverteilung der Neigunswerte. Die Resultate wurden für einen weiten Bereich an Windgeschwindigkeiten und Windwirklängen, sowohl untereinander verglichen, als auch mit der vorhandenen Live-Auswertung der ISG. Mit den ermittelten Werten wurde auch die Fetch-Abhängigkeit der mittleren quadratischen Neigung untersucht, welche Informationen über die Entwicklung eines Wellenfeldes enthält.

Außerdem wurden die Neigungsbilder unter Zuhilfenahme von Bandpassfiltern in Bilder zerlegt die entweder die Neigungen der Gravitationswellen oder der Kapillarwellen beinhalten. Durch das Trennen von Gravitations- und Kapillarwellen war es möglich deren Häufigkeitsverteilungen der Neigungen getrennt zu untersuchen.

Contents

1. Introduction

One important process in the global carbon cycle is air-sea gas exchange, because the ocean is both, sink and source of atmospheric CO_2. Gas exchange at the water surface is a mass flux and is parameterized by the transfer velocity k which mainly depends on near-surface turbulence and therefore also on wind and waves (amongst others, see e.g. Kiefhaber (2014)).

To get a better understanding for the air-sea gas exchange and the transfer velocity k, the Aeolotron, a large annular wind-wave facility was set up in the Institute of Environmental Physics in Heidelberg. Using different measurement methods, insight is gained in the physical processes at the air-water interface.

One technique developed and applied there is the Imaging Slope Gauge (ISG), which is a refractive system that measures the surface slope of the wavy water surface. From the recorded slope data it is possible to determine mean square slope of the wave field. This parameter is interesting because Jah and Frew et al. (2004) found, that the mean square slope is a better parameter for the description of air-water transfer rates than the conventional wind speed parameterizations.

There are three different approaches for the calculation of mean square slope from slope images. One of those methods is already implemented as a live evaluation, which is printing out values of mean square slope during the measurement. Due to this on-line evaluation the algorithm has to be fast and suffers some confinements e.g. in resolution.

The purpose of this thesis is, to investigate if the live evaluation is giving reliable results for mean square slope. Additionally an easy to use off-line evaluation is to be implemented in an existing Python-framework to ensure the accessibility of this important parameter. The implemented methods for the determination of mean square slope shall be compared to each other for a wide range of wind and fetch conditions. With the resulting values the fetch dependency of mean square slope is to be analyzed.

2. Theory

First, the basic physical laws of waves and hydrodynamics are given. After that the mathematical description of wave fields is explained. In the last part of this section some essential image processing routines are introduced.

2.1. Physical Laws

Navier-Stokes Equation

The basic equation for fluid mechanics is the Navier-Stokes equation, which results from fundamental conservation laws in combination with the continuity equation. A formally derivation of the Navier-Stokes equation can be found for instance in Kun,

$$\frac{\partial \vec{u}}{\partial t} + (\vec{u}\vec{\nabla})\vec{u} = -\vec{\nabla}\Phi - \frac{1}{\rho}\vec{\nabla}p - 2(\vec{\omega} \times \vec{u}) + \nu\vec{\nabla}^2\vec{u}\,. \tag{1}$$

Looking on this equation one can identify acceleration terms of different forces, acting on a viscous fluid. The terms on the left hand side represent local and convective acceleration of the fluid which indicates, that this equation holds in the Eulerian description. On the right hand side, the terms display from left to right: gravitational acceleration, pressure gradient acceleration, Coriolis acceleration and frictional acceleration.

Summing up, the Navier-Stokes equation is a momentum balance equation that describes viscous flow. Because of the non-linearity in the convection term, it is only possible to solve the above equation analytically with some simplifying approximations.

Waves on the Water Surface

From the Navier-Stokes equation, it is possible to derive some special cases of surface water waves. In the following, linear waves in irrotational, inviscid flow are roughly described. A derivation and more detailed information can be found in Kun.

Waves on the water surface can be distinguished from their main restoring forces. *Gravity waves* are surface displacements which are restored by gravity. Their wavelength is in the range from several hundred meters to centimeters.
Capillary waves are those whose main restoring force is surface tension. Thus they have low curvature radius, corresponding to short wavelengths from only a few mil-

limeters.
Waves with wavelengths in between gravity waves and capillary waves are called gravity-capillary waves.

The dispersion relation of phase velocity c and wavelength λ for small-amplitude waves in deep water is given by

$$c(\lambda) = \sqrt{\frac{g\lambda}{2\pi} + \frac{2\pi\sigma}{\rho\lambda}}\,, \tag{2}$$

where g is the acceleration of gravity, ρ the density of the fluid and σ the surface tension. For wavelengths that are dominated by one restoring force, expression (2) can be simplified further, using only the left term for gravity waves or the right term for capillary waves (Rocholz, 2008).

2.2. Description of Wave Fields

Observing not only one wave i.e. as solution of a specific equation but looking at an area of a wavy water surface induced by the wind, one can barely identify a regular pattern. Instead the surface seems to be the superposition of a huge number of waves with different wavelengths, amplitudes and phase speeds. Phillips (1977) described it that way:

> *The waves found on the surface of the sea are almost always random in the sense that the detailed configuration of the surface varies in an irregular manner in both space and time. Only the various statistical measures of the motion can be regarded as significant observationally or predictable theoretically.*

There are two ways to describe a wave field that account for the 'irregular manner'. Both possibilities are introduced below.

2.2.1. Spectral Description

Generally, a wave field can be described by the surface displacement $\eta(\vec{x}, t)$ from the mean water level, so that $\overline{\eta} = 0$. Following Phillips (1977) the wave spectrum $X(\vec{k}, \omega)$

is the Fourier transform of the autocorrelation of $\eta(\vec{x}, t)$,

$$X(\vec{k}, \omega) := \mathcal{F}[\, R(\vec{r}, \tau)\,] = \int\int\int R(\vec{r}, \tau)\, e^{-i(\vec{k}\vec{r} - \omega\tau)} \mathrm{d}\vec{r}\, \mathrm{d}\tau\,, \tag{3}$$

where $R(\vec{r}, \tau)$ is the autocorrelation function

$$R(\vec{r}, \tau) = \overline{\eta(\vec{x}, t)\, \eta(\vec{x} + \vec{r}, t + \tau)} = \mathcal{F}^{-1}[\, |\hat{\eta}(\vec{k}, \omega)|^2]\,. \tag{4}$$

The last equality is shown in Kiefhaber (2014) and is really useful, because recombining (3) and (4) leads to

$$X(\vec{k}, \omega) = |\, \hat{\eta}(\vec{k}, \omega)\,|^2\,. \tag{5}$$

So the wave spectrum is simply given by the squared absolute value of the Fourier components of surface displacement.

Another possibility for a spectral description is to characterize the wave field over the slope $s(\vec{x}, t)$ in each point, resolved in time. Actually it is easier to measure the slope of waves with short wavelength than determining their surface displacement. Following Balschbach (2000), the two quantities are related via the Nabla-Operator,

$$\vec{s}(\vec{x}, t) = \vec{\nabla}\, \eta(\vec{x}, t)\,. \tag{6}$$

One basic property of the Fourier transform is, that derivations in the spatial domain become multiplications in the Fourier domain and vice versa. Using this we can rewrite (6) to

$$\hat{\vec{s}}(\vec{k}, \omega) = -i\vec{k}\, \hat{\eta}(\vec{k}, \omega)\,. \tag{7}$$

Writing the slope spectrum $S(\vec{k}, \omega)$ in analogy to the wave spectrum, we find the following relationship:

$$S(\vec{k}, \omega) = |\, \hat{\vec{s}}(\vec{k}, \omega)|^2 = k^2\, |\, \hat{\eta}(\vec{k}, \omega)|^2 = k^2\, X(\vec{k}, \omega)\,. \tag{8}$$

2.2.2. Probability Distribution

Instead of using a spectral description of the wave field it is also possible to analyze probability distributions of slope, surface elevation or phase.

For this thesis only the distribution of slope is relevant and therefore the introduc-

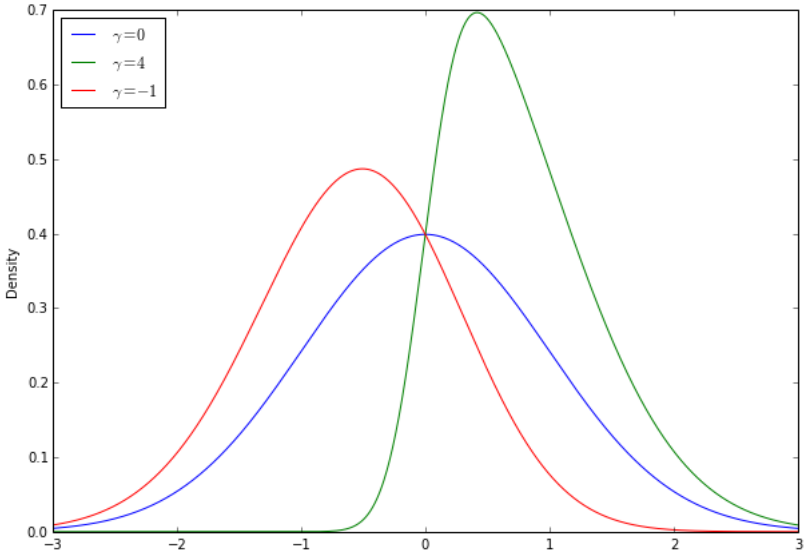

FIG 1: *Gaussian distributions with mean $\mu = 0$ and standard deviation $\sigma = 1$ but with different skewness parameters γ.*

tion of probability distributions is confined to slope distributions. For more detailed information, see i.e. Holthuijsen (2007).

Assuming linear wave theory, which implies that the principle of superposition is fulfilled and using the central limit theorem (see Rice (1995)) the resulting slope distribution is Gaussian. Due to non-linear interactions between the waves the Gaussian distribution is disturbed. Due to this the real probability density function (pdf) shows deviations from the Gaussian distribution. Another reason for this effect is, that the steepness of water waves is limited to a maximum before the waves are breaking. Additionally there are capillary waves riding almost always on the downwind side of gravity waves. This leads to a displacement of the most probable slope in positive x-direction of the distribution (Balschbach, 2000). This characteristics are mathematically described by the parameters of skewness γ and kurtosis κ.

As illustrated in figure 1, *skewness* holds for the asymmetry of a distribution. For positive skewness parameters γ the most probable value is shifted in positive x-direction, whereas for negative γ it is shifted in negative x-direction. For $\gamma = 0$ the standard Gaussian distribution is recovered. Mathematically skewness is given by the

third standardized moment

$$\gamma = \frac{\frac{1}{n}\sum_{i=1}^{n}(X_i - \mu)^3}{\sigma^3}\,, \tag{9}$$

where μ is the mean of the random variables $X_1 \dots X_n$ and σ the standard deviation, given by

$$\sigma = \left(\frac{1}{n}\sum_{i=1}^{n}(X_i - \mu)^2\right)^{\frac{1}{2}}\,. \tag{10}$$

.

Kurtosis κ is given by the fourth standardized moment and describes how 'peaked' the distribution is, compared to a standard Gaussian distribution.

$$\kappa = \frac{\frac{1}{n}\sum_{i=1}^{n}(X_i - \mu)^4}{\sigma^4} \tag{11}$$

Using the parameters of skewness and kurtosis it is possible to define a model function which fits to the measured pdf of slope data. The model function is based on a standard Gaussian distribution with Hermite polynomials as correction terms and is given in one dimension by,

$$p(s) = A \cdot \exp\left(-\frac{(s-\mu)^2}{2\sigma^2}\right)\left[1 + \frac{1}{6}\gamma H_3 + \frac{1}{24}\kappa H_4 + \dots\right], \tag{12}$$

where the H_n are Hermite polynomials of degree n. There is no physical justification for (12), but it was proposed by Longuet-Higgins (1963), used by Kiefhaber (2014) and it accounts well for the shape of the slope distribution.

2.2.3. Mean Square Slope

Mean square slope (σ_{mss}) is defined as the variance of the surface slope and is a measure for the roughness of the water surface,

$$\sigma_{mss} = \sigma_x^2 + \sigma_y^2\,. \tag{13}$$

The σ_x^2 and σ_y^2 are the squared standard deviations (see (10)), which are called variances, in along- and crosswind direction.

It is possible to simply add the variances in along- and crosswind direction to achieve the two-dimensional information, if those directions are the principal axes of the sys-

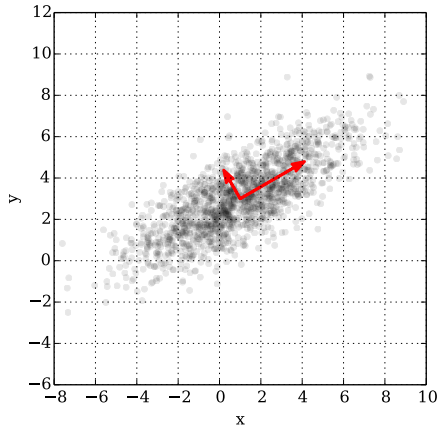

FIG 2: *Sample points with a two-dimensional Gaussian distribution. Because the x and y components have non-vanishing covariance, the variances σ_x^2 and σ_y^2 do not fully describe the distribution.*

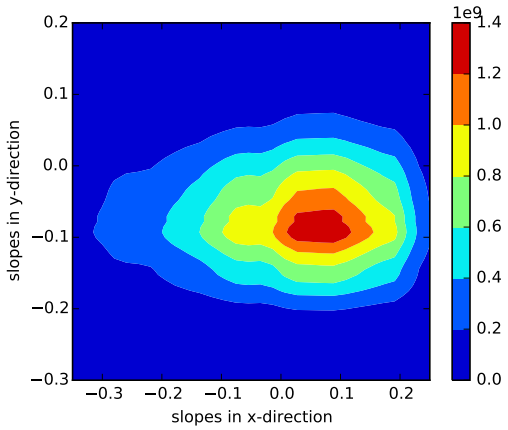

FIG 3: *Measured distribution of slopes at 12.6Hz wind condition and 7m fetch. The covariance of the x- and y-components is zero and therefore the distribution is fully described by the variances σ_x^2 and σ_y^2.*

tem, which is given in this case.

This means, that the covariances in x- and y-direction are zero and therefore the distribution is fully described by the variances σ_x^2 and σ_y^2. Figure 2 and 3 illustrate this behavior. In Fig.2 a random distribution with non-vanishing covariances is created, whereas in Fig.3 a representative two-dimensional distribution of slope values is shown. It is apparent that the covariance of the slopes in x- and y-direction is vanishing or at least is close to zero.

The idea of using σ_{mss} is to link gas transfer to wave-related processes of surface turbulence generation and surface renewal events. Although there is no theoretical justification for the use of σ_{mss}, it was shown by Jah that it correlates well with the transfer velocity k.

In practice, measurements are limited in one way or the other. Additionally σ_{mss} can be determined in multiple ways (following Kiefhaber (2014)), each with its own advantages and drawbacks. All methods listed below refer to recorded slope data.

- *Statistics*: It is simple to calculate the variances of a recorded set of slope data. Unfortunately it is not possible to exactly measure slope values without upper limit. Due to this the calculated σ_{mss} is underestimated. Additionally capillary waves with very small wavelengths can not always be resolved. This leads to further underestimation of σ_{mss}, because the small capillary waves typically have the highest slopes.

- *Probability Distribution*: The σ_{mss} can also be determined by fitting the probability density function (pdf) to the distribution. The huge problem is, that it is not possible to write down an analytical function that represents the pdf. But it is possible to find an appropriate model function that can be fitted to the slope distribution. One possible model function,which will be used within the scope of this thesis is introduced in (12). The main advantage of determining σ_{mss} by fitting the distribution is, that the fit function extrapolates the higher slope values that cannot be measured.

- *Spectral Integration*: It is also possible to calculate σ_{mss} in the Fourier domain, which is simply the Integral over all wave numbers. Determining σ_{mss} this way has the same limitations as adding the variances of the data set. One advantage of spectral integration over the statistical methods is, that the contribution of different wavelengths to σ_{mss} can be investigated easily.

2.3. Image Processing

In this section some basics of image processing used in this thesis are presented. The most important tool is the discrete Fourier transform. Directly connected with Fourier transform is Parseval's theorem, as well as window functions. Furthermore, a Gaussian smoothing filter was applied on the data and is introduced below.

Discrete Fourier Transform

The sensor elements of a camera are usually organized on a regular rectangular grid so that an image with regular rectangular picture elements (pixel) is received. To apply Fourier transform to such an image, the continuous form needs to be discretized.

Let the picture have $M \cdot N$ pixel with the pixel length Δx in both spatial directions.

Then the discrete Fourier transform (DFT) of a two dimensional signal g_{mn} is

$$\hat{g}_{uv} = \frac{1}{MN} \sum_{n=0}^{N-1} \left(\sum_{m=0}^{M-1} g_{mn}\, e^{-\frac{2\pi i m u}{M}} \right) e^{-\frac{2\pi i n v}{N}} . \tag{14}$$

This representation is equivalent to the continuous form, but the integral is replaced by the sum. The inverse discrete Fourier transform is then given as

$$g_{mn} = \sum_{v=0}^{N-1} \left(\sum_{u=0}^{M-1} \hat{g}_{uv}\, e^{\frac{2\pi i m u}{M}} \right) e^{\frac{2\pi i n v}{N}} . \tag{15}$$

The normalization factor of $\frac{1}{MN}$ is usually multiplied to the inverse transform, but is here used differently. The advantage of doing this is that Parseval's theorem (see below) can be applied without any further normalizing.

Parseval's Theorem

Parseval's theorem states, that the squared sum of a signal amplitude $x(n)$ is the same as the squared sum of its Fourier transform. For the discrete Fourier transform introduced above, the relation is

$$\sum_{n=0}^{N-1} |x(n)|^2 = \sum_{k=0}^{N-1} |\mathcal{F}\left[x(n)\right]|^2 = \sum_{k=0}^{N-1} |\hat{x}(k)|^2 . \tag{16}$$

This guarantees energy conservation when calculating the spectrum of an image.

Windowing

One requirement of discrete and bounded Fourier transform is, that the transformed signal is periodic. If it is not, artifacts are created at the edges of the image which leads to high frequencies in Fourier domain. To avoid such artifacts, it is possible to use window functions that decrease to zero at the edges of the image. Multiplying the signal with such a window function makes the signal periodically continuable.

The window used in this thesis is the Hann function and is given in one dimension by

$$w(n) = \frac{1}{2}\left[1 - \cos\left(\frac{2\pi n}{N}\right)\right], \tag{17}$$

where N is the sequence length. To apply the Hann window to an image, a two

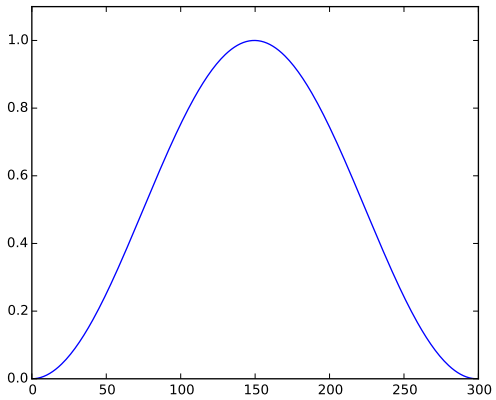

FIG 4: *One-dimensional Hann function for a sequence length of* $N = 300$.

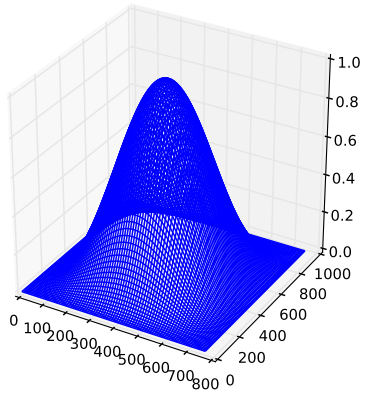

FIG 5: *Two-dimensional Hann function for an image shape of* $960 \times 768 px$.

dimensional function is required

$$w(n,m) = \frac{1}{4}\left[1 - \cos\left(\frac{2\pi n}{N}\right)\right] \cdot \left[1 - \cos\left(\frac{2\pi m}{M}\right)\right], \tag{18}$$

where N, M are the dimensions of the image. The one- and two-dimensional functions are shown in figure 4 and 5.

Smoothing Filter

Smoothing an image means, that fine patterns are blurred and only larger structures remain visible.

This can be done by using a two dimensional Gaussian filter with standard deviation σ. For a given filter mask with odd length N, the maximum value of the filter is placed in the center of the mask, so that the mean μ is equal to zero. Also considering the normalization, the $N \times N$ filter becomes,

$$G_{2D} = \frac{1}{\sqrt{2\pi}\sigma} \cdot \exp\left(-\frac{n_x^2 + n_y^2}{2\sigma^2}\right), \tag{19}$$

with $-\frac{N-1}{2} \leq n_x, n_y \leq \frac{N-1}{2}$ the positions in the filter mask. From this formula a fil-

ter mask with variable length and standard deviation can be created. Convolving the resulting filter mask with an image produces the smoothed image, where smaller structures are blurred. More detailed information as well as some examples on Gaussian filters can be found in Jähne (2005).

3. Generation and Preprocessing of the Data

In this section the experimental setup as well as the preprocessing of the recorded image sequences is briefly explained.

3.1. Imaging Slope Gauge

The Imaging Slope Gauge (ISG) was developed in Heidelberg and further improvement is still ongoing. With this device it is possible to detect small scale wind-water waves with high temporal and spatial resolution. The ISG that recorded the data evaluated in this thesis is installed at the Aeolotron in Heidelberg and is described in detail in Kiefhaber et al. (2014). Here only the basic mode of operation is introduced.

Imaging Setup

Figure 6 shows a schematic of the ISG at the Aeolotron in Heidelberg. The camera is observing the water surface from above and the water body is illuminated from below with a programmable LED light source. On its way to the camera the light rays are passing a Fresnel lens that guarantees telecentric alignment, before they are refracted at the water surface corresponding to Snell's law

$$n_a \sin(\alpha) = n_w \sin(\beta)\,, \tag{20}$$

where $n_a \approx 1$ and $n_w \approx 1.33$ are the refractive indexes of air and water.

Due to the fact, that the light source is installed in the focal plane of the Fresnel lens, all rays with an exit angle α correspond to exactly one position of the light source. In other words, slopes of the water surface belong to distinct positions on the illumination screen independent of their position on the water surface. This important relation is sketched in Figure 7.

Extracting Slope Data

In the images recorded by the camera, one pixel belongs to a spatial position of the water surface. The numerical value of this pixel corresponds to the incoming intensity, that originates from the light source. If the light source is coded with a spatial brightness gradient, it is possible to relate the intensity of a pixel to the slope of the corresponding point of the water surface.

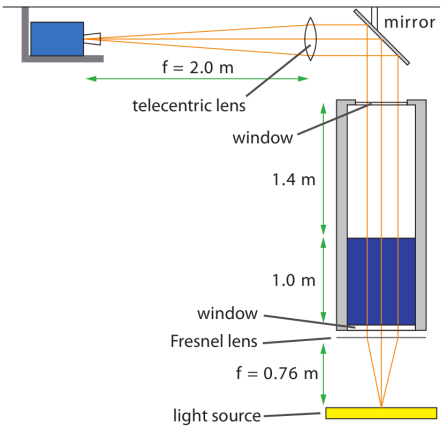

FIG 6: *Wave imaging setup at the Aeolotron. Source: Kiefhaber et al. (2014)*

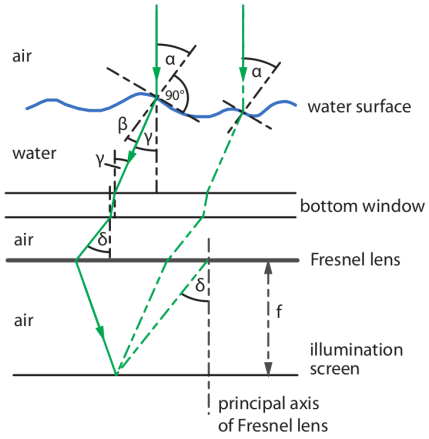

FIG 7: *Ray geometry of the Imaging Slope Gauge. Source: Kiefhaber et al. (2014)*

To get the slope of the surface in both spatial directions, two intensity gradients (one in each direction) would be necessary. However, in the used setup, four different gradients (shown in Figure 8) are applied. This has the additional advantage that lens effects of the water surface as well as inhomogeneities of the light source can be minimized by calculating normalized intensities (see section 3.2).

3.2. Data Preprocessing

The routines for normalization, calibration and interpolation of the ISG image sequences were implemented in Python by Klein (2015) and used for the evaluation in this thesis. In the following the main steps that are necessary to get slope information from a raw ISG image sequence are explained.

Dark Image

First a dark image is subtracted from every image of the sequence. This is done to reduce electronic artifacts of the camera (Jähne, 2005). The dark image is generated by averaging images that are recorded with covered camera lens.

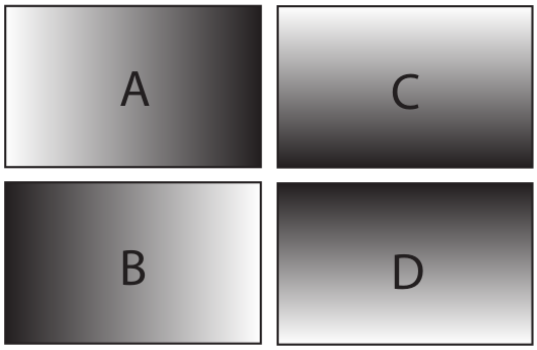

FIG 8: *Brightness Gradients of the ISG. Source: Kiefhaber et al. (2014)*

Normalization

The normalized intensities are

$$I_x = \frac{A - B}{A + B} \tag{21}$$

$$I_y = \frac{C - D}{C + D} \tag{22}$$

with A, B, C, D an image sequence, illuminated with the four intensity gradients like shown in figure 8. The advantage of the normalized intensities is, that lens effects and inhomogeneities of the light source are eliminated by normalizing to the total intensity.

Calibration

For the assignment of absolute slope values to the appropriate intensities in each pixel, a look up table (LUT), similar to the one introduced in Rocholz (2008), is created. For the generation of the LUT a calibration sphere is used. For this sphere the slope value in every point is known, so that it is possible to relate slope values directly to recorded intensities. The details of the calibration process are for example explained in Klein (2015) and Reith (2014).

Interpolation

During the above explained processes of recording, normalizing and calibrating the images, bad pixels can occur. Those bad pixels can be determined by thresholding, and are saved in a separate array. In the last step of preprocessing they are interpolated by an algorithm that was originally developed by D'Errico (2004) and matched

to the ISG data by Klein (2015). Details concerning the algorithm as well as a test of suitability can also be found in Klein (2015).

Below, the full preprocessing routine is illustrated in a flow chart.

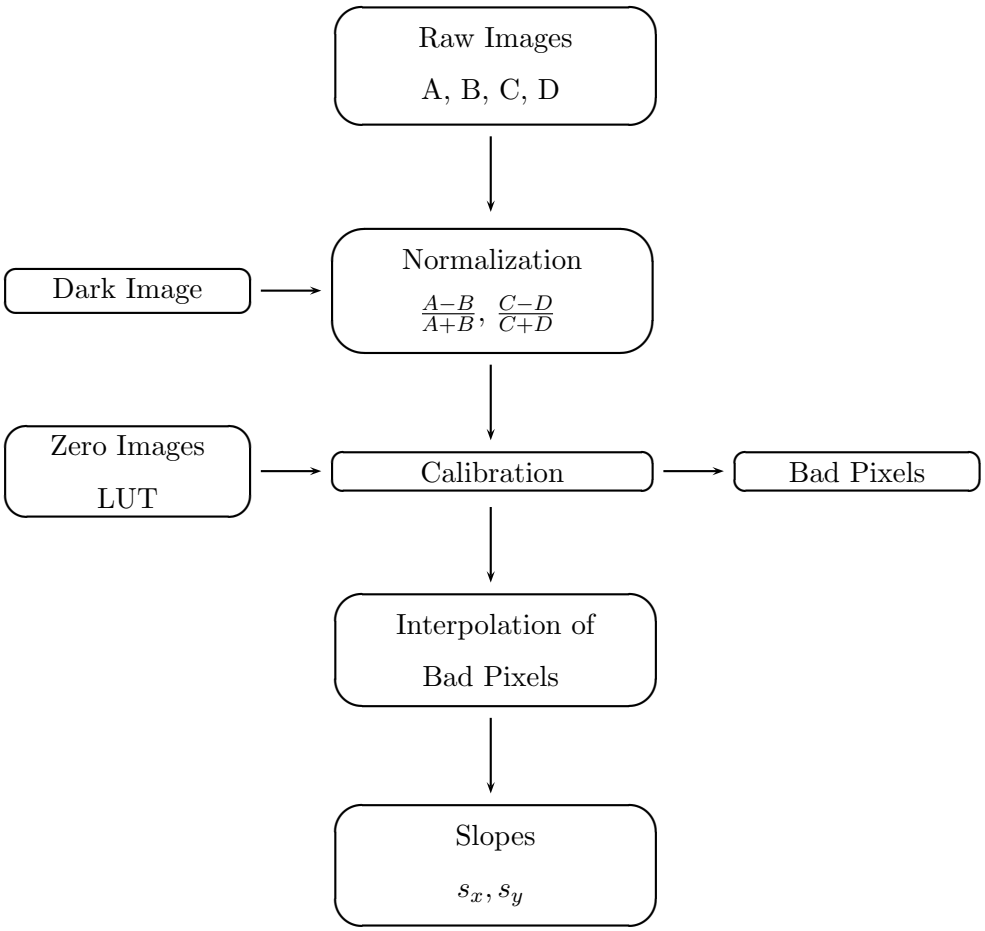

4. Data Evaluation

The intensity images recorded with the ISG are evaluated in Python. The preprocessing routines (see section 3.2) are reused to generate calibrated slope images.

In the scope of this thesis, the Python framework for the ISG images is extended by some specific processing routines which calculate σ_{mss} from the slope-images. Additionally the resulting slope distributions are analyzed in more detail. In this section the methods are explained and difficulties are discussed.

4.1. Statistics

Following the definition of σ_{mss} (see (13)) it seems simple to calculate the variances of both slope components s_x and s_y, add them up and get a result. Then the σ_{mss} would be

$$\sigma_{mss} = \sigma_x^2 + \sigma_y^2 \,, \tag{23}$$

with the general definition of variance

$$\sigma^2 = \langle s^2 \rangle - \langle s \rangle^2 \,. \tag{24}$$

In the special case of investigating the slope of a water surface the above formula can be simplified further, because the mean slope of the water surface is expected to be zero, so that $\langle s_x \rangle^2 = \langle s_y \rangle^2 = 0$, and therefore,

$$\sigma_{mss} = \langle s_x^2 \rangle + \langle s_y^2 \rangle \,. \tag{25}$$

However in the case of evaluating data from the ISG at the Aeolotron this assumption is not quite true. Instead it holds, that $\langle s_y \rangle > 0$, whereas $\langle s_x \rangle \approx 0$ as expected. This is due to the circularity of the facility and is discussed below in more detail.

The first problem with (23) is now, that the image sequences from which the σ_{mss} is calculated contains about 2000 images with each a size of 960×768px. Due to this huge amount of numbers it is not possible to read all data at once into the RAM to apply Pythons built-in function for variance to the data. This means that we need to calculate the variance for smaller fractions of the data set and then average over the determined values to become the overall variance.

For the sake of compatibility with the preprocessing routines we do not decompose

the data set into a few subsets, but we first calculate the variance for each image with the built-in function of Python and then average over all determined values. Mathematically, this is

$$\sigma_x^2 = \frac{1}{T}\sum_{t=1}^{T}\underbrace{\left(\langle s_x^2\rangle_t - \langle s_x\rangle_t^2\right)}_{built-in\ function} = \frac{1}{T}\sum_{t=1}^{T}\langle s_x^2\rangle_t - \underbrace{\frac{1}{T}\sum_{t=1}^{T}\langle s_x\rangle_t^2}_{>0}, \tag{26}$$

with T the number of images, $t = 1, \ldots, T$. The same holds for the slope in y-direction. The right term represents the mean slope of one image squared and then averaged over all images so that it will be a positive number, because the mean slope in a single image does not necessarily need to be zero. But, as explained above, the mean slope over the whole sequence $\frac{1}{T}\sum_{t=1}^{T}\langle s_i\rangle_t$ is expected to be zero and therefore, we need to correct for the error made in (26). This can be achieved by adding the falsely subtracted value after the calculation of the averaged variances.

The true σ_{mss} then is

$$\sigma_{mss} = \sigma_x^2 + \sigma_y^2 + \frac{1}{T}\sum_{t=1}^{T}\langle s_x\rangle_t^2 \; + \frac{1}{T}\sum_{t=1}^{T}\langle s_y\rangle_t^2 \,. \tag{27}$$

This calculation can be easily realized in Python by using the built-in functions that determine mean and variance of a given array.

Applying (27) on the preprocessed sequences still leads to an overestimation of σ_{mss} compared to the values determined with the methods presented below in section 4.2 and section 4.3. This is, as mentioned above, due to the circularity of the facility which causes centrifugal forces that act on the rotating water body. Due to this the mean slope of the crosswind component is different from zero and needs to be subtracted from (27) according to (24). The same is done for the mean slope in x-direction even though the value is close to zero (order 10^{-5}). The final equation for the calculation then is

$$\sigma_{mss,corr} = \sigma_x^2 + \sigma_y^2 + \frac{1}{T}\sum_{t=1}^{T}\langle s_x\rangle_t^2 \; + \frac{1}{T}\sum_{t=1}^{T}\langle s_y\rangle_t^2 - \left(\frac{1}{T}\sum_{t=1}^{T}\langle s_x\rangle_t\right)^2 - \left(\frac{1}{T}\sum_{t=1}^{T}\langle s_y\rangle_t\right)^2. \tag{28}$$

A more detailed mathematical derivation of (28) can be found in appendix A.1.

In the flow chart below the full working routine is illustrated.

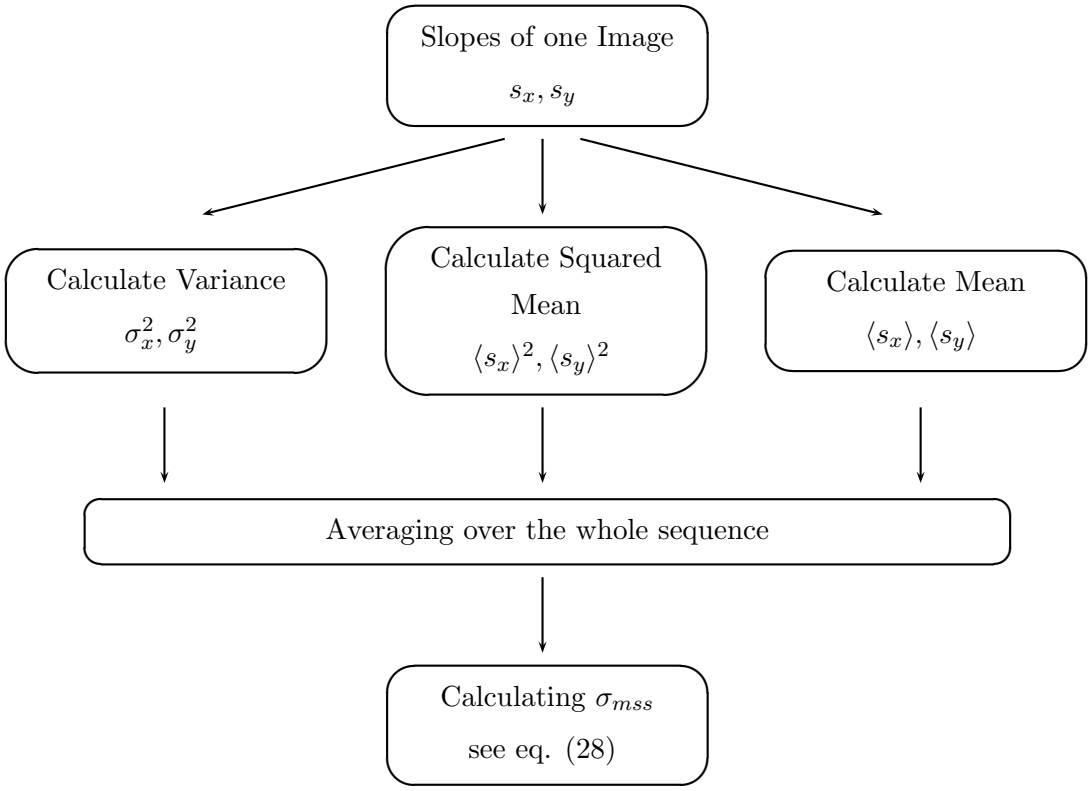

4.2. Spectral Integration

Like introduced in section 2.2.3, σ_{mss} can also be determined by integrating the slope power spectrum over all wavelengths. The slope power spectrum (see (8)) is given as

$$S(\vec{k}, \omega) = |\, \hat{s}(\vec{k}, \omega)|^2 \,. \tag{29}$$

This means, that first two-dimensional DFT is applied on every image of the sequence. The problem arising here is, that the images have sharp edges whereas one of the requirements of Fourier Transform is the periodicity of the transformed signal. To allow for this fact, the images are first multiplied with a window function, like it was introduced in section 2.3 before the Fourier transform is applied. This leads to

$$\hat{s}_x(u, v) = \mathcal{F}\,[\, s_x(m, n) \cdot w(m, n)\,]\,, \tag{30}$$

with u and v the pixel indices of the Fourier transformed image, $s_x(m, n)$ a preprocessed slope image and $w(m, n)$ the two-dimensional window function as introduced

in (5). The same formula is valid for the slope images $s_y(m,n)$.

The interest of doing DFT, is the value of the integral over each image. Due to this it is necessary to consider the impact of the window function. To do this in a efficient way, Parseval's theorem (see section 2.3) is utilized, which states the energy conservation of Fourier transform. This offers the possibility to multiply the signal in the spatial domain with a window function, and correct the amplitudes later in the Fourier domain.

According to (29) we calculate the squared absolute value of the Fourier transformed images which before were multiplied with the window function. This means that we need to correct for the impact of the squared Hann function.

Integrating the squared Hann function (17) in one dimension over the image length N yields

$$\frac{1}{N}\int_0^N w(n)^2\,dn \;=\; \frac{1}{N}\int_0^N \frac{1}{4}\left(1-\cos\left(\frac{2\pi}{N}\cdot n\right)\right)^2 dn \;=\; \frac{3}{8}\,. \tag{31}$$

To correct for the impact of the window function on the image, the amplitudes must be multiplied with the inverse of the result, which is $\frac{8}{3}$. The Hann function applied on the image sequence is a two dimensional window, so that the correction factor for the spectrum is $\frac{64}{9}$.

In the next step, the squared absolute value of the Fourier transformed and corrected image is integrated over all wave numbers, which is simply the sum over all pixel values. Like in section 4.1 it must be taken into account, that the wave field is observed only on a small surface patch. Due to this, the mean value in one single image can be different from zero, though one would expect the mean slope of the whole water surface to be zero.

Because the integration is applied to the spectrum, which is the squared Fourier transform of the slope images (see section 2.2.1) it is not possible for the mean values to compensate for each other when averaging over a large sequence of statistically independent images. To account for this fact, the mean value, which is in the Fourier transformed image simply the pixel at the position $u = v = 0$ is set to zero. This is equivalent to subtracting the mean of a certain image from the integrated value of the same image.

Averaging over all the images and taking all the corrections into account yields,

$$\sigma^2_{x,corr} = \frac{64}{9}\frac{1}{T}\sum_{t=0}^{T-1}\left(\left(\sum_{u=0}^{M-1}\sum_{v=0}^{N-1}|\hat{s}_x(u,v)|^2\right)_t - |\hat{s}_x(0,0)|^2_t\right), \tag{32}$$

with T the number of images in one sequence and u and v are the indices for the pixels in one Fourier transformed image. For the slope in y-direction the calculations are analogue, so that $\sigma_{mss} = \sigma_x^2 + \sigma_y^2$.

The full processing routine is illustrated in the flow chart below and is equally done for the slopes in x- and y-direction.

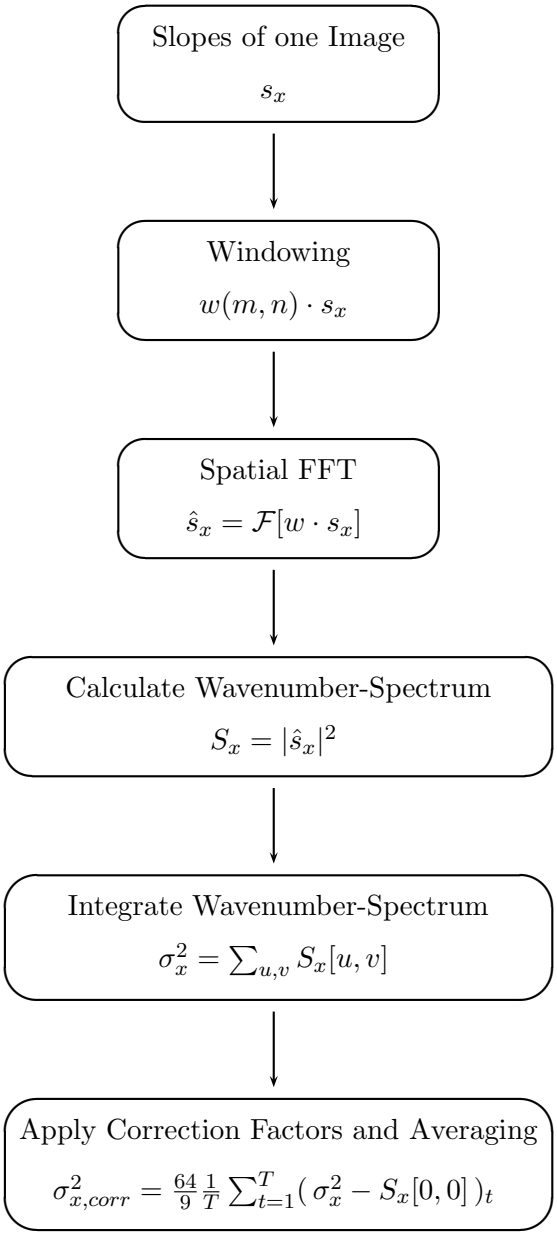
Slopes of one Image
s_x
Windowing
$w(m,n) \cdot s_x$
Spatial FFT
$\hat{s}_x = \mathcal{F}[w \cdot s_x]$
Calculate Wavenumber-Spectrum
$S_x = |\hat{s}_x|^2$
Integrate Wavenumber-Spectrum
$\sigma_x^2 = \sum_{u,v} S_x[u,v]$
Apply Correction Factors and Averaging
$\sigma_{x,corr}^2 = \frac{64}{9}\frac{1}{T}\sum_{t=1}^{T}(\,\sigma_x^2 - S_x[0,0]\,)_t$

4.3. Probability Distribution

As already mentioned in section 2.2, it is difficult to determine σ_{mss} by fitting a pdf to the slope distribution, because the analytical function for the pdf is not known. There are different approaches that try to describe slope distributions, which mostly base upon the standard Gaussian distribution. In this thesis, equation (12) is assumed to be a reasonable model function,

$$p(s) = A \cdot \exp\left(-\frac{(s-\mu)^2}{2\sigma^2} \right) \left[1 + \frac{1}{6}\gamma H_3 + \frac{1}{24}\kappa H_4 + \dots \right]. \tag{33}$$

This is a standard normal distribution with mean μ and standard deviation σ which is modified by Hermite polynomials H_n of order n. The parameters γ and κ account for skewness and peakedness of the investigated distribution.

This function is fitted to the slope distributions with A, μ, σ and γ as fit parameters. The Hermite polynomial of fourth order is skipped (and so the fifth fit parameter κ), because praxis has shown that including a fifth parameter does not improve the result significantly. Due to this, it is a greater advantage to have less fit parameters in the model function.

In this thesis the one-dimensional model function (33) up to the third Hermite polynomial is fitted to a one-dimensional distribution (separately for x- and y-direction) and later the results are superimposed to one two-dimensional slope distribution. This is possible because the chosen directions x (alongwind) and y (crosswind) are the principal axis of the investigated system, such that the slopes are statistically uncorrelated. As already presented in section 2.2.3 this is clearly visible from the two dimensional slope distributions, which all look similar to the one shown in figure 3 and vary only in width and shape but not in orientation. To investigate this quantitatively, the normalized cross correlation of the two distributions in x- and y-direction is calculated, which is

$$\rho_{xy} = \frac{\frac{1}{n}\sum_{i=1}^{n} \left((s_{x,i} - \langle s_x \rangle) \cdot (s_{y,i} - \langle s_y \rangle) \right)}{\sigma_x \sigma_y}, \tag{34}$$

with s_x the slope value in one pixel, $\langle s_x \rangle$ the mean slope of the whole sequence and σ the standard deviation (see (10)). Like already mentioned above, ρ_{xy} is normalized which means that the result of (34) is a number between -1 and 1.

For the data sets evaluated in the scope of this thesis we find $|\rho_{xy}| < 0.2$. This

indicates only very weak correlation, so that the above assumption is valid, notably because in most cases we find $|\rho_{xy}| < 0.1$ and only for some measurement conditions the correlation is about 0.2.

At certain conditions of wind speed and fetch the slope distribution has bimodal shape. For this regimes the model function (33) was adapted in a way, that a superposition of two functions (with each individual fit parameters A, μ, σ, γ) was used for the fit.

Because the standard Gaussian distribution is modified with the Hermite polynomial to represent a reasonable model function, the variance is no longer a direct fit parameter, but needs to be calculated separately. This is realized by first determining the mean μ' from the normalized model function by calculating

$$\mu' = \int s \cdot p(s)\, ds \tag{35}$$

where $p(s)$ is the fitted model function with the parameters determined by the fit. Knowing the mean μ', the variance σ'^2 can be determined by solving the integral,

$$\sigma'^2 = \int (s - \mu')^2\, p(s)\, ds\,. \tag{36}$$

The total σ_{mss} is then given as the sum of the variances for the slope distributions in x- and y-direction,

$$\sigma_{mss} = \sigma_x'^2 + \sigma_y'^2\,. \tag{37}$$

Analysis of Slope Distributions

Due to the fact that the shape of the measured slope pdfs is varying with wind and fetch conditions, it seems interesting to further investigate the distributions.

To get some more information about the wave field, band pass filters (see section 2.3) are applied to the slope images. The standard deviation of the Gaussian filter is chosen to be 15. This leads to an image where the small structures of the capillary waves are blurred and only the slopes of the gravity waves are visible (low pass filter). To get the information of the capillary waves, the blurred image is subtracted from the original image, which results in an image containing only the slope data of waves

with short wavelengths (high pass filter).

Figure 9, 10 and 11 represent the result of the procedure, applied to an exemplary image at conditions of 10Hz wind and 21m fetch, where figure 9 is the original image and figure 10 and 11 are the separated slopes of gravity and capillary waves.

This procedure of separating the long and the short wavelengths is done for a whole sequence of images to yield slope distributions for gravity waves and capillary waves separately. The evolution of these pdfs with increasing wind speed or fetch obtains information about the development of the wave field at the corresponding condition.

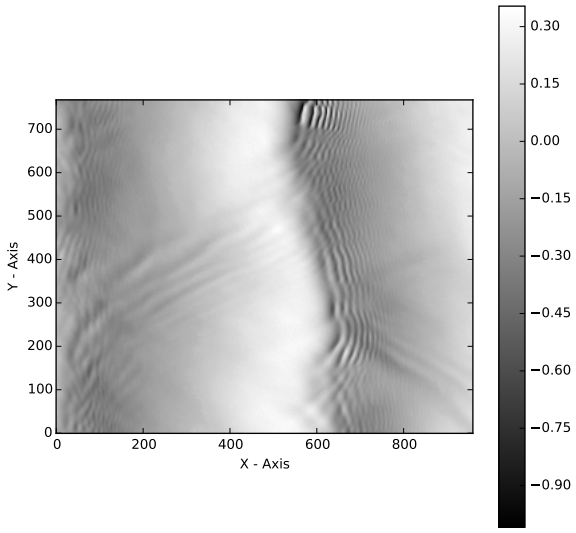

FIG 9: *Slope image at* $10Hz$ *wind and* $21m$ *fetch.*

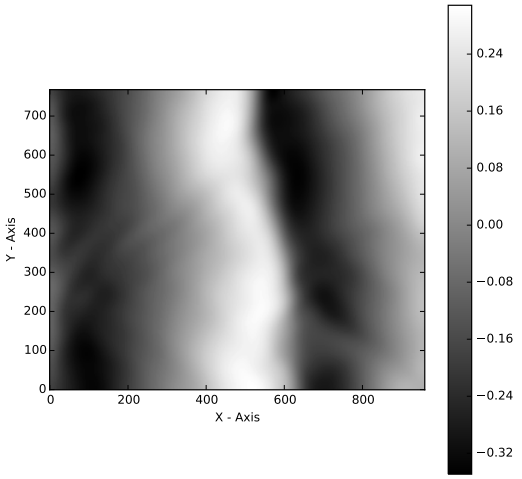

FIG 10: *Slopes of gravity waves extracted from figure 9 using a Gaussian blurring filter.*

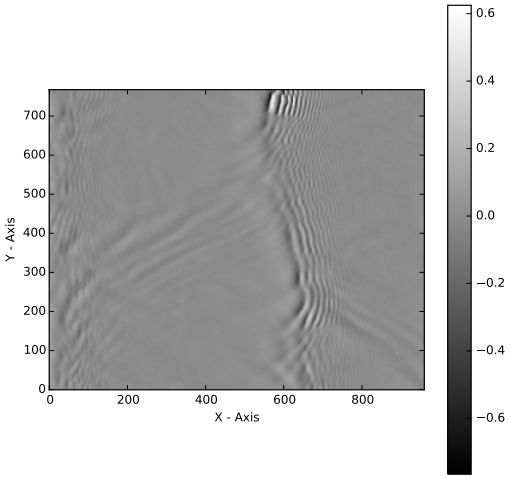

FIG 11: *Slopes of capillary waves determined by subtracting figure 10 from figure 9.*

5. Results

In the scope of this thesis the analysis of wave measurements is performed. The data was recorded at the Heidelberg Aeolotron by Jakob Kunz and Christine Kräuter in June and July 2015. Different data sets are evaluated, which include five wind speeds under varying fetch conditions and a wide range of different wind speeds with unlimited fetch. The calculated values that are used for the plots presented in this section are listed in appendix A.2 in tables 1 and 2.

In the following, the results will be presented and discussed.

Characterization of Wind Speed

For the characterization of wind speed over a wave field, there are several definitions that are used for different purposes. For the evaluation of the slope images in this thesis, there are two relevant parameters that characterize the wind speed condition in the Aeolotron. One is the frequency which is used as a setting for the electronics that control the wind generator given in Hz and the other is u_{ref}, given in m/s which is measured with a vane anemometer in the facility approximately 1m above the water surface. The value of u_{ref} for each measurement is important to know, because dependent on the wave field the mean wind speed u_{ref} can vary for a fixed wind condition given in Hz. It was not possible in the scope of this thesis to estimate the magnitude of this variations due to the fact that until the end of this thesis not all the values for u_{ref} had been available.

The measured values for u_{ref} are presented in appendix A.2 for the conditions where the wind sensor was working properly. For the further discussion of the results the wind condition given in Hz is used to characterize wind speed. For more detailed information about the wind field in the Aeolotron, the different parameterizations of wind speed and the corresponding measurements see Bopp (2014).

5.1. Evaluation Methods

Figure 12 shows σ_{mss} plotted against fetch for fixed wind conditions of 10.0Hz, 12.6Hz, 15.8Hz, 19.9Hz and 25.1Hz. The range of σ_{mss} used in the plots is adapted to the total range that appears in the different measurement for comparability. The four curves in the plots represent different evaluation methods, which are described in section 4, except for the live-calculation (dark blue). The live-calculation of σ_{mss}

was implemented by Daniel Kiefhaber and is in principle the same as the statistical method. The difference is, that this value is printed out during the measurement and is determined by calculating the variance over the last 600 recorded slope images for each recorded image. The value for σ_{mss} given in this thesis as result of the live evaluation is the last value printed out at the end of the measurement. The temporal trend of σ_{mss} over a whole measurement sequence has been investigated and we found it to be very stable, so that choosing the last value is a reasonable representation of the determined values for the conditions that were investigated in this study.

In the plots shown in figure 12 it is conspicuous, that the values determined by fitting the measured pdf with the model function don't match the values from the other methods. Nevertheless, in figure 13, which shows the calculated σ_{mss} for conditions with unlimited fetch, the values for the fitting method are in good agreement with the values from live-calculation and the statistics method. Here the calculation in the Fourier domain (red graph) seems to underestimate σ_{mss} for higher wind speeds. This behaviour can also be observed for wind speeds greater than 15.8Hz in figure 12, where the red curve lies beneath the other two lines.

Mean Square Slope at unlimited Fetch Conditions

Figure 13 represents the calculated values for σ_{mss} at conditions with unlimited fetch. Obviously there are no big differences between the different evaluation methods. In contrast to the limited fetch conditions, here the fitting method is in better agreement to the other methods. The specific observation in this plot is the value for σ_{mss} at 12.6Hz wind condition, which seems to underestimate the real value, if a smooth graph is expected. Due to the fact, that all evaluation methods match together, there must either be some underlying physical process or some systematic error in the measurement is responsible for this effect.

To investigate which of the assumptions is more likely, some values from Aeolotron measurements performed in 2011 (taken from Reith (2014)) are plotted in the same figure. The value from Reith (2014) for 12.6Hz wind condition is higher than the value calculated in this thesis and seems much more reasonable compared to the neighbouring values. This leads to the assumption that a systematic error in the measurement is more likely than some underlying physical process.

It is known that surfactants on the water surface are damping the wave field and

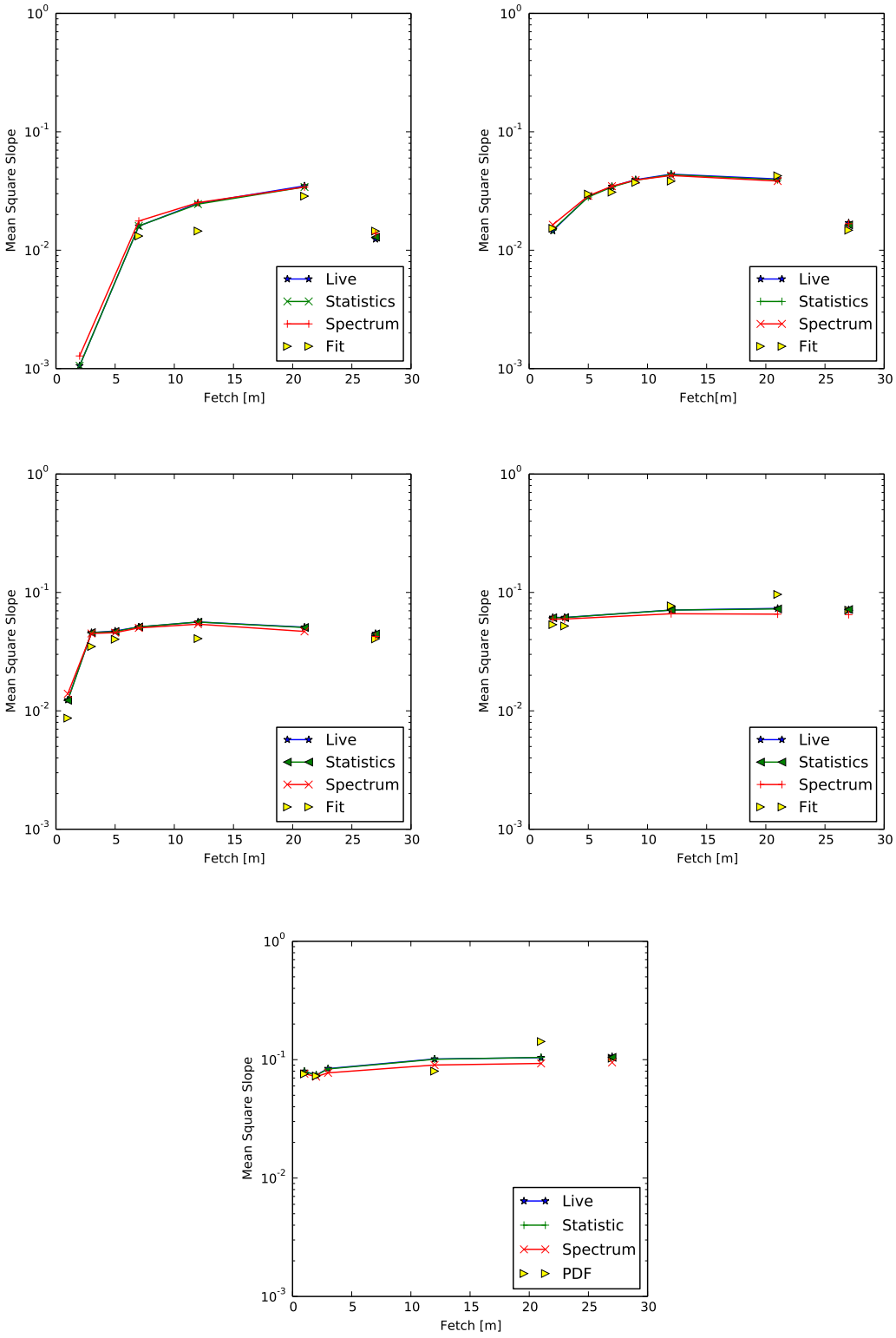

FIG 12: *Fetch dependence of σ_{mss} at 10Hz (upper left), 12.6Hz (upper right), 15.8Hz (center left), 19.9Hz (center right) and 25.1Hz (lower plot) wind condition in semilogarithmic scale. The last data point in the each plot represents the σ_{mss} at conditions with unlimited fetch and the four graphs represent the results of the different evaluation techniques (see section 4).*

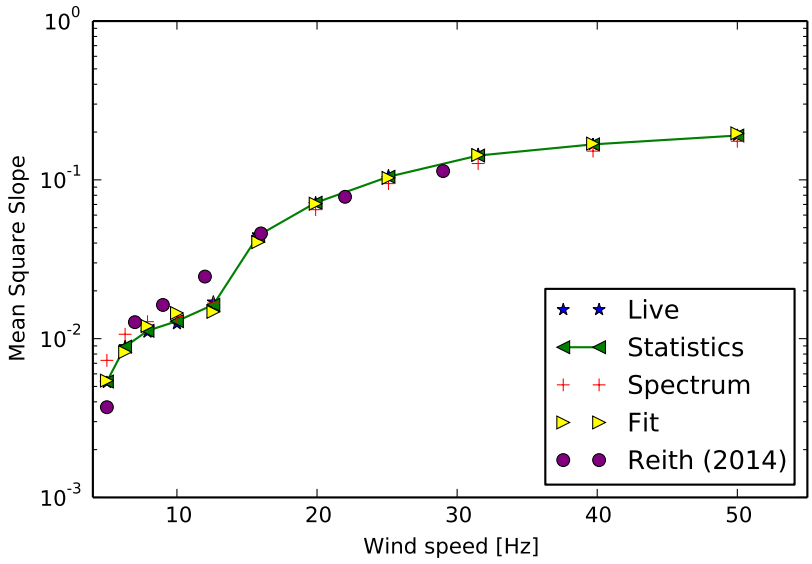

FIG 13: σ_{mss} *as a function of wind speed under conditions with unlimited fetch. The purple dots are values taken from literature (Reith, 2014).*

therefore lead to a decrease in σ_{mss}. Additionally the development of surfactants during the measurement is a common problem when investigating water waves. Due to this we assume that the water surface was not perfectly clean during the measurement with unlimited fetch at 12.6Hz wind condition. This indeed is a physical process but due to the fact that the measurements evaluated in this thesis are performed with clean water surface this is also a systematic error in the measurement. This assumption cannot be proven, but in Krall (2013) the same behaviour has been observed and interpreted the same way.

5.1.1. Discussion: Fit-Method

In plots 12 and 13 the values for σ_{mss} determined by the fitting method do not match the other values under fetch-conditions, but yield good results for conditions with unlimited fetch.

This behaviour is quite unclear, especially because there is no trend visible in the deviations. Actually, it is not always easy to fit the measured pdf and for a few distributions it was not possible to get a converging fit. Figure 14 - 16 show some of the fitted model functions and represent typical shapes of the distributions and the

problems that appear for fitting the model function.

From the plots shown, it becomes evident that it is possible to describe the slope pdf with the model function (33), even if the parameter for peakedness is skipped as explained in section 4.3. In figure 14 on the right it is visible that the fitted model function lacks peakedness compared to the measured pdf. On the other hand in figure 15 on the right the model function also fits the peakedness of the distribution quite well. As already described in section 4.3 it is very difficult to achieve a converging fit with the additional parameter of peakedness in the model function. Additionally the fitted model functions including the peakedness-parameter are rarely more peaked than the fits with the simpler model function.

Another characteristic of some of the pdfs is the bimodal shape which can be seen in figure 15 on the left and in figure 16 on the right. It is also visible that the chosen model function can deal with this bimodal shape if it is adapted as discussed in section 4.3. It is also visible that the fits do not match perfectly, but they still fulfill our criterion that the residuals have a maximum deflection of 0.1, which are 10% of the maximum value of the pdf. This means that figure 16 on the right shows the worst evaluated fit. For even greater deviations of the model function from the measured pdf, the pdf is called 'not fittable'.

Another typical behaviour of fitted model functions is illustrated in figure 15 on the left, where the positive tail of the model function shows oscillations. This is due to the Hermite polynomials which are multiplied to the normal distribution to achieve a reasonable model function. In most cases it was possible to eliminate this effect by varying the fit-parameters but sometimes the best result was only a maximal reduction of the oscillations. However, also in this case the residuals are in the required range and the fit is used for the calculation of σ_{mss}.

In figure 16 on the left the fitted pdf for conditions with unlimited fetch at 31.5Hz wind condition is shown. Compared to the other distributions this plot shows several smaller ledges on the flanks of the measured pdf. This shape is typical for distributions of unlimited fetch conditions that were investigated in this thesis. As a consequence the fitted model function cannot represent this pdf in great detail because it has smooth flanks, which leads to continuously scattering residuals.

As illustrated with the help of the plots 14 - 16 it is possible to fit different shapes of measured pdfs quite satisfactory. For both cases (limited and unlimited fetch) there are quite good fits (15 on the right and 14) but also some poor results (15 on the left

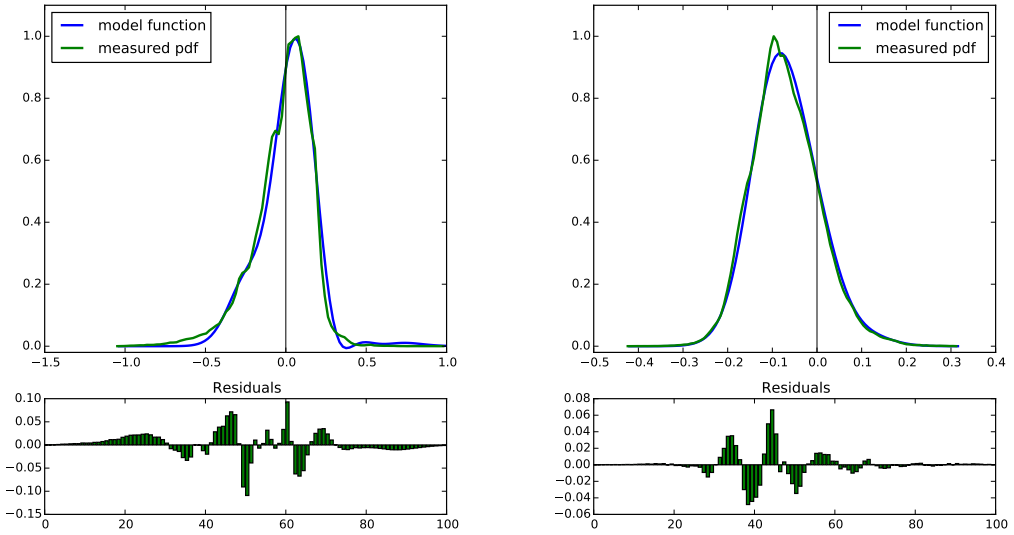

FIG 14: *Fits of the model function* (33) *to the measured slope pdf at* 12.6*Hz wind condition and* 7*m fetch. The pdf is normalized to the maximum value for comparability. On the left the pdf in x-direction is shown and on the right the pdf in y-direction.*

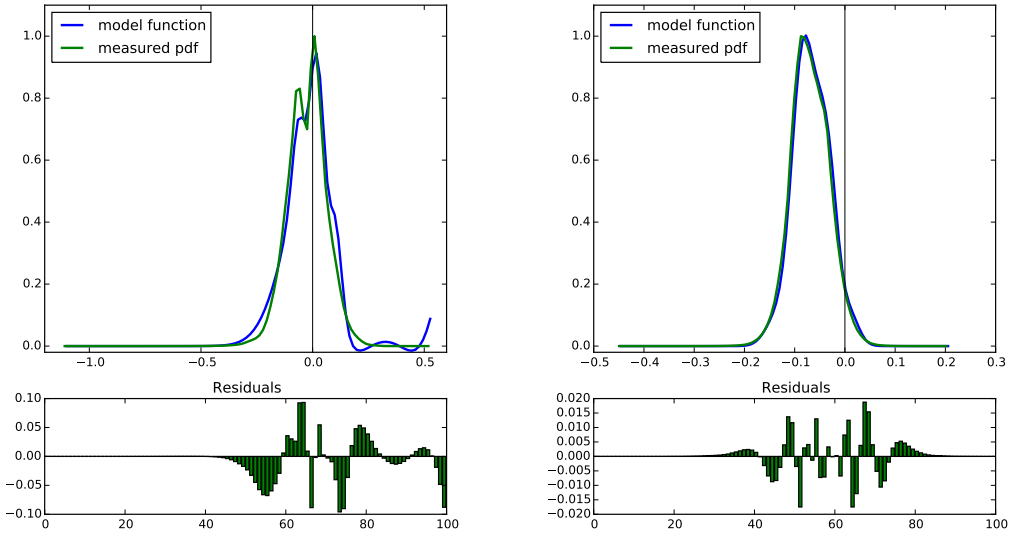

FIG 15: *Fits of the model function* (33) *to the measured slope pdf at* 6.3*Hz wind condition and unlimited fetch conditions. The pdf is normalized to the maximum value for comparability. On the left the pdf in x-direction is shown and on the right the pdf in y-direction.*

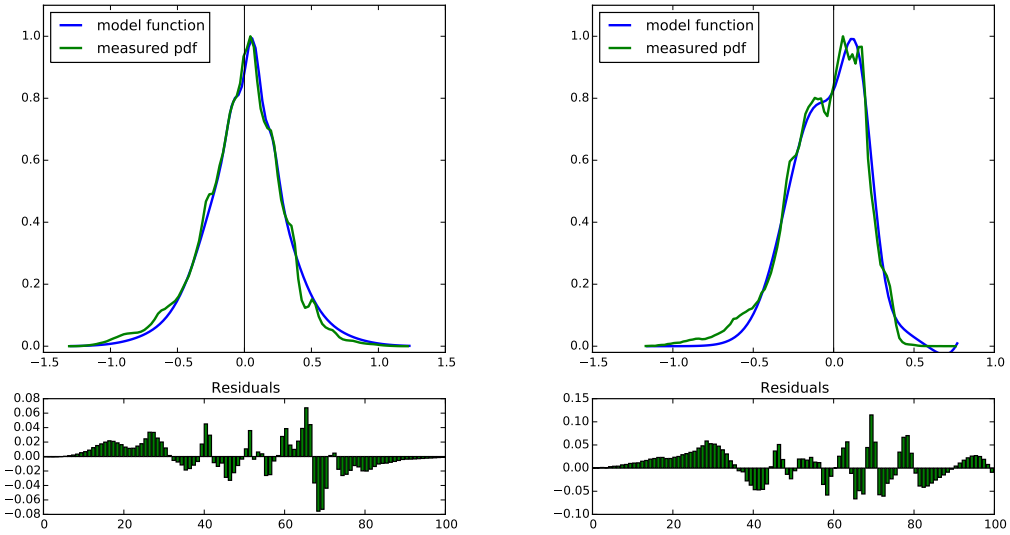

FIG 16: *Fit of the model function* (33) *to the measured slope pdf in x-direction at* 31.5*Hz wind condition and unlimited fetch conditions (on the left) and* 19.9*Hz wind and* 12*m fetch (on the right). The pdf is normalized to the maximum value for comparability.*

and 16 on the right). Due to this it is still unclear why the fit-method yields good results of σ_{mss} for conditions with unlimited fetch but shows clear deviations for fetch conditions.

5.1.2. Discussion: Spectral Integration

For the resulting plots of σ_{mss} (figure 12 and 13) it is noticeable that the values which are calculated in the Fourier domain (see section 4.2) are lying slightly beneath the values calculated with the statistics method. The deviations are at maximum 10% and increase with wind speed and fetch. Following Kiefhaber (2014) the result of spectral integration and the statistics method should be exactly the same.

After investigating all possible sources of errors, a mistake in the subtraction of the mean slope has been identified. The evaluation routine is calculating (according to section 4.2)

$$\sigma^2_{x,corr} = \frac{64}{9}\frac{1}{T}\sum_{t=1}^{T}(\sigma_x^2 - S_x[0,0])_t\,, \tag{38}$$

with σ_x^2 the integral over the slope power spectrum S_x for one image, and $S_x[0,0]$ the mean of the slope power spectrum of the picture t. Calculating the σ_{mss} this way is exactly the same as averaging over momentary variances of single images, which is discussed in section 4.1 and appendix A.1 to yield the wrong result for the global variance.

The physical explanation why this calculation cannot be correct is, that the mean slope of one single image should contribute to σ_{mss}, while the global value of mean slope is expected to be zero. However, in the Aeolotron especially the cross wind component of the global mean slope is different form zero due to the centrifugal forces acting on the water body so that we must correct for it. Mathematically the global mean in the Fourier domain is

$$\langle \hat{s} \rangle_{glob} = \frac{1}{T} \sum_{t=1}^{T} \hat{s}\,[0,0]\,, \tag{39}$$

with $\hat{s}$ the Fourier transform of a slope image and its mean at the position $u = v = 0$.

Before doing the Fourier transform on each image we multiply the slope image with the window function (18). In section 4.2 it was argued, that the impact of the window function on the amplitudes must be corrected with the corresponding normalization factor (see (31)).

However, the value for the global mean must be corrected before calculating the square, so that it is necessary to determine the corresponding normalization factor by solving the integral,

$$\frac{1}{N} \int_0^N w(n)\, dn = \frac{1}{N} \int_0^N \frac{1}{2} \left(1 - cos\left(\frac{2\pi}{N} \cdot n \right) \right) dn = \frac{1}{2}\,. \tag{40}$$

The normalization factor for the Hann function in 1D therefore is 2. Due to the fact that we apply the 2D-function on the image, the normalization factor we use is 4.

This means, that the correct calculation for σ_{mss} in the Fourier domain is $\sigma_{mss} = \sigma_x^2 + \sigma_y^2$ and

$$\sigma_x^2 = \frac{64}{9} \frac{1}{T} \sum_{t=1}^{T-1} \left(\sum_{u=0}^{M-1} \sum_{v=0}^{N-1} |\hat{s}_x[u,v]|^2 \right)_t - \left| \frac{4}{T} \sum_{t=1}^{T} \hat{s}_x[0,0]_t \right|^2 , \tag{41}$$

with T the sequence length and $\hat{s}[u,v]$ the Fourier transform of the slope image mul-

tiplied with the window function.

Due to the fact, that the calculations are very time expensive only a few data sets at present have been evaluated a second time, with the new correction implemented. For the reevaluated data sets we find a good agreement with the values calculated from the statistical method. The deviations are at maximum 3% from the statistical value.

Those deviations can possibly result from the linear calibration which is used in the preprocessing routine, which converts intensity images into slope images. This assumption arises, because the Fresnel lens placed between the light source and the water body (see figure 6) is not an ideal lens which leads to errors especially at the edges of an image. This results in a non homogeneous slope signal, even though the wave field is assumed homogeneous. When applying the window function (5) to the images the amplitudes at the edges are damped before the spectrum is calculated and integrated to yield σ_{mss}. This way the more precisely calibrated pixels from the center of the image are contributing stronger to the resulting value of σ_{mss} than the pixels at the image borders. In the statistical method all pixels of the image are used with their full amplitudes for the calculation of σ_{mss}, which can cause a deviation from the true value due to aberrations.

In the scope of this thesis it was not possible to investigate this further, though there are some simple ideas how to approximate the errors that are caused by the linearity of the calibration. One possibility is to calculate σ_{mss} for the center and the edges of the images separately. From the relation between those two values it should be possible to estimate the errors.

5.1.3. Discussion: Statistics & Live-Evaluation

It becomes clear from figures 12 that the determined values for the statistics method don't differ from those of the live evaluation. This is not surprising insofar as both methods are calculating the variances of the data sets to yield σ_{mss}. The difference however is, that the statistical method determines σ_{mss} from the complete sequence of recorded images (see section 4.1), whereas the live evaluation is determining σ_{mss} during the measurement.

If the ISG is running in the statistical mode which produces statistical independent images, there is enough time for one image to be calibrated and evaluated before the

next image is recorded. The calibration used in the live evaluation is similar to the work flow presented in section 3, but uses only a resolution of 1/8 compared to the calibration that is done in the scope of this thesis. This means that for one slope value in the live calibration there are 8 slope values in the calibration, used in this thesis.

Another reason why differences between the two methods can possibly occur is, that the live calculation is using poorer statistics, because it needs to be fast. In the live evaluation the σ_{mss} is calculated over a sequence length of 600 images which corresponds to about 20% to 50% of the sequence length used for the statistical method. Due to those confinements (in resolution and sequence length) of the live evaluation, one objective of this thesis was if the resulting value for σ_{mss} is just approximating the real value or if the result is reliable.

With the results presented in this thesis it is verified that the live-evaluation of σ_{mss} yields correct results.

5.2. Analysis of Slope Distributions

As described in section 4.3 the images of one sequence are separated in gravity and capillary waves to yield distributions for longer and shorter wavelengths separately. The pdfs of gravity waves show remarkable differences between limited and unlimited fetch conditions, whereas the pdfs of the capillary waves look very similar.

Figures 17 and 18 represent the distributions of gravity and capillary waves in semilogarithmic scale at conditions with unlimited and limited fetch, respectively. The distributions are presented dimensionless as a function of s/σ, with s the slope-value and $\sigma = \sqrt{\sigma_{mss}}$ the root mean square.

As can be seen in figure 17 the slope pdf for gravity waves roughly follows a Gaussian distribution. This is a typical observation for slope pdfs of gravity waves at unlimited fetch conditions. The distribution of the capillary waves is much broader than the pdf of the gravity waves and therefore also broader than a normal distribution. It is consistent with general observations (e.g. Kiefhaber (2014)), that the small scale waves typically have the highest slope values. In figure 18 the slope distribution of capillary waves is also broader than the pdf of the gravity waves, but the two distributions look very different from those in figure 17.

Comparing the slope distributions of gravity waves, which are represented by the blue curves, one observes that at conditions with limited fetch the pdf has a plateau

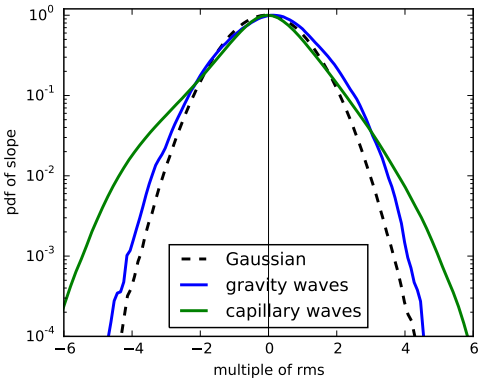

FIG 17: *Slope pdfs of separated gravity and capillary waves for unlimited fetch conditions at* $50Hz$ *wind speed, normalized to the maximum value for comparability. As a reference the Gaussian distribution is plotted. The pdfs are plotted dimensionless in semilogarithmic scale.*

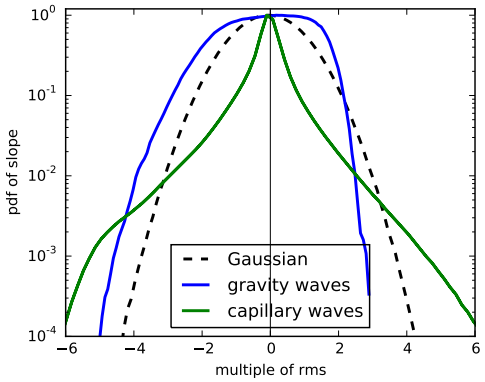

FIG 18: *Slope pdfs of separated gravity and capillary waves for* $7m$ *fetch and* $15.8Hz$ *wind speed, normalized to the maximum value for comparability. As a reference the Gaussian distribution is plotted. The pdfs are plotted dimensionless in semilogarithmic scale.*

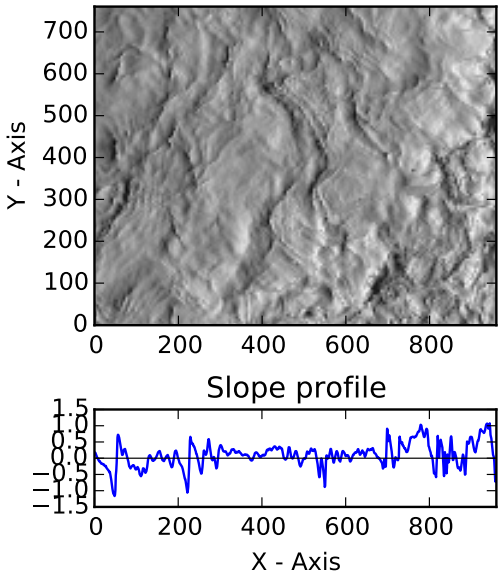

FIG 19: *Slope image with slope profile, corresponding to the distribution shown in figure 17 at unlimited fetch conditions and* $50Hz$ *wind speed. The slope profile is taken at row* 400.

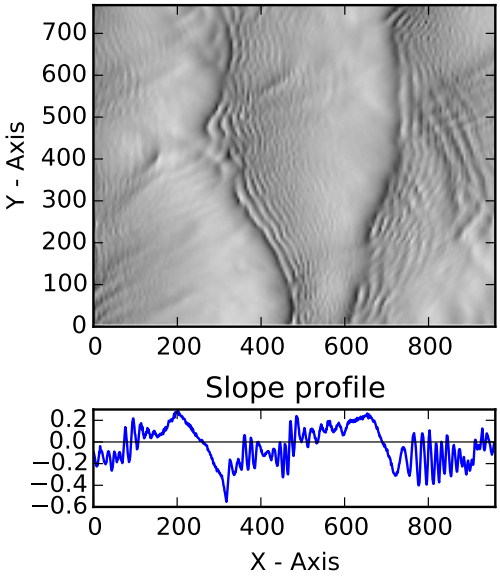

FIG 20: *Slope image with slope profile, corresponding to the distribution shown in figure 18 at* $7m$ *fetch conditions and* $15.8Hz$ *wind speed. The slope profile is taken at row* 400.

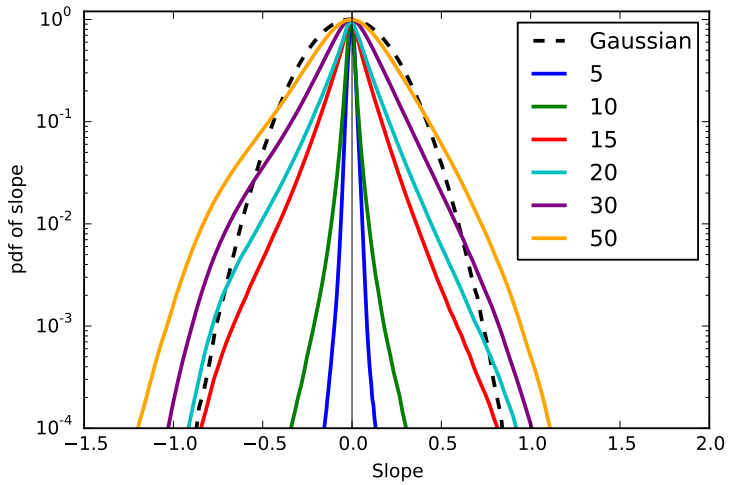

FIG 21: *Measured slope pdfs of capillary waves for different wind speeds in semilogarithmic scale, normalized to their maximum value. The legend identifies wind conditions in Hz. As a reference a Gaussian distribution with standard deviation* $\sigma = 0.2$ *and mean* $\mu = 0$ *is plotted.*

around slope zero and looks much more asymmetric than the pdf at unlimited fetch conditions. This shape seems reasonable when taking into account that for conditions with limited fetch a dominant wave length can be observed. The wave field is no longer a superposition of all possible wavelengths as it is the case for unlimited fetch conditions.

Additionally, for both pdfs of gravity waves it can be observed that the deviation from the Gaussian distribution is a little more pronounced for small positive slopes. This shape accounts for the front-back asymmetry of the wave profiles, which is illustrated in figures 19 and 20. The conditions for the represented slope images are the same as those for which the slope pdfs are shown in figures 17 and 18. In the slope profiles the tendency that small positive slopes occur more frequently than small negative slopes is visible. Like shown in figures 17 and 18 this pattern is more pronounced for the fetch-limited condition.

Investigating the pdfs of capillary waves for the two conditions shown in figures 17 and 18 the distributions look quite different. However, this effect mainly depends on wind speed but not on different fetch lengths. For both cases (limited and unlimited

fetch) the distributions of capillary waves are really peaked for small wind speeds and become broader for higher wind speeds. Figure 21 shows the pdfs of capillary waves for different wind speeds at conditions with unlimited fetch in semilogarithmic scale. It can be observed, that the range of detected slope values is growing broader with wind speed.

The evolution of shape with increasing wind speed seems reasonable, because at very small wind speeds (5Hz - 10Hz) only a few capillary waves are riding in front of the waves crest. Those small ripples have the highest slopes at the corresponding condition, which leads to a broad basis of the distribution. The sharp peak at slope zero represents the relatively rare occurrence of the capillary waves in those wind regimes, so that slope zero occurs very often compared to higher slope values. With the increase of wind speed the relative occurrence of slope zero is decreasing, because the overall surface roughness is increasing which explains the broadening of the distributions at medium slope values.

Directly linked to this effect, is the observation of a step in the broadness of the distribution which occurs from wind conditions of 10Hz to 15.8Hz. One possible explanation for this effect is the beginning of micro scale breaking of the capillary waves. At 10Hz wind condition no micro scale breaking is detected, whereas at 15.8Hz wind condition it is frequently observed (personal communication with Angelika Klein).

Another interesting observation in figure 21 is the transition of the pdfs of higher wind speed conditions ($\geq$ 19.9Hz) at a slope value of approximately -0.8. For slope values between zero and -0.8 the pdf nearly has a linear shape in the logarithmic scale, whereas for slope values less than -0.8 the graph looks more similar to the normal distribution. See the Gaussian distribution ($\sigma = 0.2$ and $\mu = 0$) plotted in the dashed line, appearing as a parabola in the logarithmic scale. For positive slopes this behaviour is not that pronounced, but also visible.

A more detailed investigation and interpretation of the distributions shown in figure 21 is not possible in the scope of this thesis, but seems worth to be done in the future.

5.3. Fetch Dependence of σ_{mss}

Figure 22 shows the fetch dependency of σ_{mss} for different wind speed conditions. The surface roughness increases with wind speed as well as with increasing fetch.

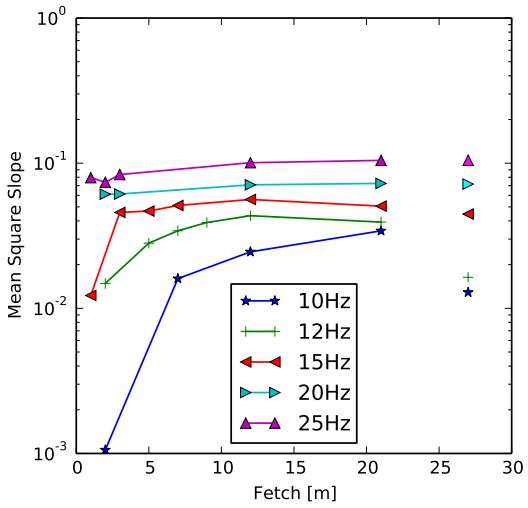

FIG 22: *Fetch dependency of σ_{mss} for all measured wind conditions. The graphs show the values calculated with the statistical method. The last data point represents σ_{mss} at conditions with unlimited fetch.*

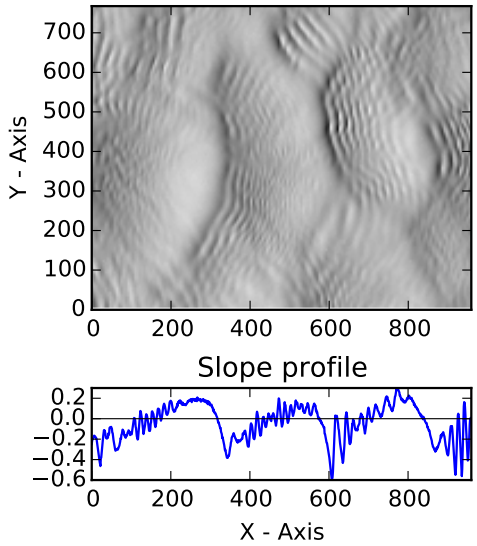

FIG 23: *Typical slope image at 12.6Hz wind and 12m fetch. The corresponding profile is taken at row 400.*

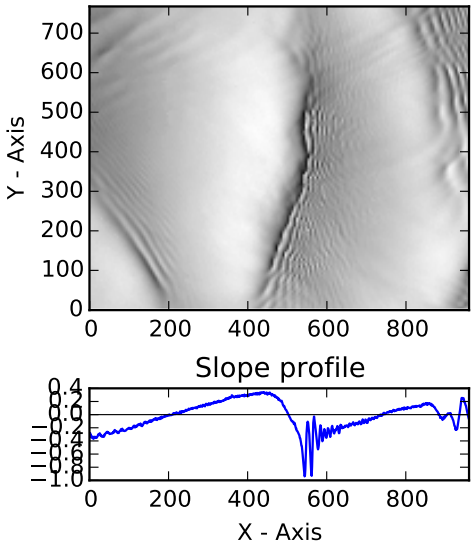

FIG 24: *Typical slope image at 12.6Hz wind and 21m fetch. The corresponding profile is taken at row 400.*

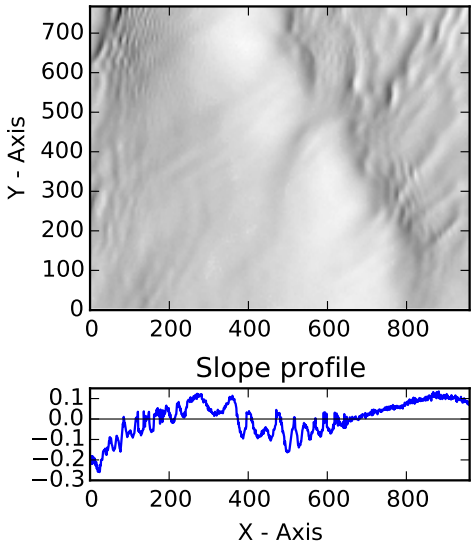

FIG 25: *Slope image at 12.6Hz wind and unlimited fetch conditions. The corresponding profile is taken at row 300.*

An interesting observation in the plot is that for lower wind conditions, up to 12.6Hz (green and blue graph) the value for σ_{mss} at unlimited fetch conditions (the last data point) is significantly smaller than for the measurements at 21m fetch.

A similar behaviour was observed by Caulliez (2013), who calculated the dominant wave steepness ak_d under fetch limited conditions. The graph of ak_d over fetch first increases before it is then dropping at a fetch length of 26m.

The physical process causing this effect is the general evolution of a wave field, which is well known from the experimental point of view, but not perfectly understood theoretically due to the nonlinear interactions.

Figure 23, 24 and 25 represent typical slope images with corresponding slope profiles at 12.6Hz wind and different fetch conditions. The images correspond to the last three data points of the green graph in figure 22, which means that σ_{mss} is increasing from figure 23 (12m fetch) to figure 24 (21m fetch) and is then significantly smaller in figure 25 (unlimited fetch). From the slope profiles this effect becomes directly clear, because the range of occurring slope values is much smaller for unlimited fetch conditions than for those with limited fetch.

The evolution of a wave field is really complex and experimental observations are described in more detail in Caulliez and Guérin (2012). What can be seen even in the sample images 23 and 24 is, that with increasing fetch (and also with increasing wind speed) the dominant wave length of the gravity waves becomes larger, therefore the wave length of the parasitic capillaries decreases and the range of slope increases. This is happening from figure 23 to figure 24, where additionally the slope is increasing. For still larger fetches (or higher wind speeds) it can be observed, that more and more different wave lengths are superposing, which results in a stationary wave field for conditions with unlimited fetch.

6. Conclusion & Outlook

6.1. Conclusion

In this thesis, existing data sets have been evaluated to verify the live evaluation and to analyze the fetch dependency of mean square slope.

The evaluated data was recorded with the Imaging Slope Gauge (ISG), which is installed at the Aeolotron (see section 3.1) and the resulting images have been preprocessed using the routines of normalization, calibration and interpolation, which were already implemented in Python (see section 3.2).

The preprocessing routines result's are slope images, from which mean square slope (σ_{mss}) has been calculated. Three different methods have been implemented, which are, (i) calculation of the variance, (ii) integration of the slope power spectrum and (iii) fitting the slope pdf with a model function (see section 4). The implementations are utilizing successive processing routines, such that it is now possible to do the calculations on a computer with limited memory. However, the first attempts of successive evaluation were defective especially due to the non zero mean slope in crosswind direction at the Aeolotron. The errors have been investigated and corrected (see sections 4.1 and 4.2 and appendix A.1).

With the determined values of σ_{mss} it was possible to verify the live evaluation (see section 5.1.3). However, the live evaluation presupposes that the slope calibration is processed and reliable at the time of measurement, which is not always possible. If this is not the case σ_{mss} can be obtained from the evaluations developed in this thesis.

The implemented methods showed consistent results for σ_{mss} at unlimited fetch conditions. However, for fetch limited measurements the fitting method is scattering around the results determined by the other methods. This behaviour is still unclear and the question could not been solved within the scope of this bachelor thesis.

Analyzing fetch dependency of σ_{mss} it has been observed, that for fetch limited conditions at medium wind speeds up to 15.8 Hz, σ_{mss} has higher values for large fetches than for unlimited fetch. It was possible to give a reasonable physical explanation for this observation with the general evolution of a wave field (see section 5.3).

The slope probability distribution functions (pdfs) show significant deviations from a Gaussian distribution as well as from the used model function. Due to this for gravity and capillary waves have been separated in the images by applying band pass filtering (see section 4). With this method it was possible to investigate the distributions for

gravity and capillary waves individually. It was found, that the pdfs of gravity waves approximately follow a Gaussian distribution whereas the distributions of capillary waves show strong deviations from the normal law (see 5.2). However, the pdf for slope of capillary waves shows an interesting evolution in shape with increasing fetch, worthwhile further investigation.

6.2. Outlook

With the evaluation and analysis done so far lots of ideas arise about how complementary investigations could be performed, which however can not be part of this bachelor thesis due to the temporal confinement.

- In addition to the fetch limited measurements, it would be interesting to record ISG sequences of the temporal evolution of the wave field (at starting wind). For a sufficient number of such measurements it would be possible to compare the results to those of the fetch limited measurements (spatial evolution).

- It would be interesting to investigate the small differences in σ_{mss} between the spectral integration and the calculation of the variances. Possibly the accuracy of the linear calibration can be approximated from those differences (see section 5.1.2).

- The slope pdfs for different measurement conditions as well as the separated distributions of gravity and capillary waves are not analyzed in-depth in this thesis (see section 5.2). A more exhaustive investigation and interpretation of the shapes and their evolution with wind and fetch seems worthwhile.

  A correlation of the shapes of the distributions with micro scale breaking is currently under research.

- A more detailed statistical investigation of the wave field could be performed. The higher cumulants could be calculated from the measured pdf of slope to relate them to typical wave profiles at certain fetch conditions and therefore get a deeper understanding about the evolution of a wave field.

References

Balschbach, G. W.: Untersuchungen statistischer und geometrischer Eigenschaften von Windwellen und ihrer Wechselwirkungen mit der wasserseitigen Grenzschicht, URL `http://archiv.ub.uni-heidelberg.de/volltextserver/2473/`, 2000.

Bopp, M.: Luft- und wasserseitige Strmungsverhältnisse im ringförmigen Heidelberger Wind-Wellen-Kanal (Aeolotron), Masterarbeit, Institut für Umweltphysik, Universität Heidelberg, Germany, URL `http://www.ub.uni-heidelberg.de/archiv/17151`, 2014.

Caulliez, G.: Dissipation regimes for short wind waves, J. Geophys. Res., 118, 672–684, doi:10.1029/2012JC008402, URL `http://dx.doi.org/10.1029/2012JC008402`, 2013.

Caulliez, G. and Guérin, C.-A.: Higher-order statistical analysis of short wind wave fields, J. Geophys. Res., 117, C06 002–, doi:10.1029/2011JC007854, 2012.

D'Errico, J.: Impaint NaN's, In: mathworks.com, URL `http://www.mathworks.com/matlabcentral/fileexchange/4551-inpaint-nans`, 2004.

Frew, N. M., Bock, E. J., Schimpf, U., Hara, T., Haußecker, H., Edson, J. B., McGillis, W. R., Nelson, R. K., McKenna, S. P., Uz, B. M., and Jähne, B.: Air-sea gas transfer: Its dependence on wind stress, small-scale roughness, and surface films, vol. 109, doi:10.1029/2003JC002131, 2004.

Holthuijsen, L. H.: Waves in Oceanic and Coastal Waters, Cambdridge Univ. Press, 2007.

Jähne, B.: Digitale Bildverarbeitung, Springer, Berlin, 6 edn., doi:10.1007/b138991, 2005.

Kiefhaber, D.: Optical Measurement of Short Wind Waves — from the Laboratory to the Field, Dissertation, Institut für Umwelt-

physik, Fakultät für Physik und Astronomie, Univ. Heidelberg, URL http://www.ub.uni-heidelberg.de/archiv/16304, 2014.

Kiefhaber, D., Reith, S., Rocholz, R., and Jähne, B.: High-speed imaging of short wind waves by shape from refraction, 9, 14 015, doi:10.2971/jeos.2014.14015, 2014.

Klein, B.: Ein Python-Framework zur Berechnung und Analyse von Wellenzahlspektren winderzeugter Wasserwellen, Bachelorarbeit, Institut für Umweltphysik, Fakultät für Physik und Astronomie, Univ. Heidelberg, 2015.

Krall, K. E.: Laboratory Investigations of Air-Sea Gas Transfer under a Wide Range of Water Surface Conditions, Dissertation, Institut für Umweltphysik, Fakultät für Physik und Astronomie, Univ. Heidelberg, URL http://www.ub.uni-heidelberg.de/archiv/14392, 2013.

Longuet-Higgins, M. S.: The generation of capillary waves by steep gravity waves., J. Fluid Mech., 16, 138–159, 1963.

Phillips, O. M.: The Dynamics of the Upper Ocean, Cambridge University Press, 2 edn., 1977.

Reith, S.: Spatio-temporal slope measurement of short wind waves under the influence of surface films at the Heidelberg Aeolotron, Masterarbeit, Institut für Umweltphysik, Universität Heidelberg, Germany, URL http://www.ub.uni-heidelberg.de/archiv/17697, 2014.

Rice, J. A.: Mathematical Statistics and Data Analysis, Duxbury Press, 2 edn., 1995.

Rocholz, R.: Spatiotemporal Measurement of Short Wind-Driven Water Waves, Dissertation, Institut für Umweltphysik, Fakultät für Physik und Astronomie, Univ. Heidelberg, URL http://www.ub.uni-heidelberg.de/archiv/8897, 2008.

A. Appendix

A.1. Corrections for Statistical Method

As discussed in section 4.1 some corrections for the calculation of σ_{mss} need to be applied when using the statistical method. Here the physical argumentation is skipped for the sake of clarity and only the mathematical reasons are presented.

The definition of σ_{mss} is

$$\sigma_{mss} = \sigma_x^2 + \sigma_y^2 \,,$$

with σ_x^2 and σ_y^2 the variances of the slope data. The variance is defined as

$$\sigma^2 = \left\langle \, (s - \langle s \rangle)^2 \, \right\rangle = \langle s^2 \rangle - \langle s \rangle^2 \,.$$

The following calculations are done for only one of the variances σ_x or σ_y and is therefore just named σ. The whole formula with the corrections applied on both spatial directions x and y is presented in (28).

In the scope of this thesis we are first calculating momentary variances for each image separately and later average those values to yield the global variance for the whole image sequence. Due to averaging we are calculating

$$\sigma_{avg}^2 = \frac{1}{T} \sum_{t=1}^{T} \left(\langle s^2 \rangle_t - \langle s \rangle_t^2 \right) = \frac{1}{T} \sum_{t=1}^{T} \langle s^2 \rangle_t - \frac{1}{T} \sum_{t=1}^{T} \langle s \rangle_t^2 \,,$$

where t is one image of a sequence with length T. The mistake that originates here is, that it holds

$$\langle s \rangle^2 = \left(\frac{1}{T} \sum_{t=1}^{T} \langle s \rangle_t \right)^2 \neq \frac{1}{T} \sum_{t=1}^{T} \langle s \rangle_t^2$$

This means, that if we want to calculate the global variance for one huge array by averaging over local variances of sub arrays, we must calculate

$$\sigma^2 = \sigma_{avg}^2 + \frac{1}{T} \sum_{t=1}^{T} \langle s \rangle_t^2 - \left(\frac{1}{T} \sum_{t=1}^{T} \langle s \rangle_t \right)^2 .$$

The advantage of this procedure compared to calculating the global variance at once is, that for a large set of images we don't need to compute $\langle s \rangle$ for all images in advance.

A.2. Calculated Values for σ_{mss}

Wind [Hz]	u_{ref} [m/s]	Δu_{ref} [m/s]	Live	Statistic	Spectrum	pdf-Fit
5	1.366	0.029	0.0053	0.00537	0.007299	0.00544
6.3	1.710	0.040	0.0089	0.008903	0.010657	0.00822
7.9	2.336	0.039	0.011	0.011207	0.012791	0.01201
10	2.992	0.042	0.0124	0.012891	0.013837	0.0145
12.6	3.789	0.049	0.017	0.016358	0.016744	0.01475
15.8	4.705	0.051	0.045	0.044612	0.042455	0.04054
19.9	5.759	0.068	0.0716	0.071778	0.064927	0.07079
25.1	7.081	0.114	0.106	0.104607	0.094733	0.10285
31.5	8.348	0.193	0.1446	0.142267	0.126731	0.14341
39.7	9.594	0.256	0.167	0.167322	0.151716	0.16916
50	11.300	0.334	0.1908	0.190159	0.175019	0.19639

Table 1: *Calculated values for σ_{mss} under varying wind speeds with unlimited fetch conditions. The values of the live-calculation are taken from the corresponding documentations of the measurements and u_{ref} was kindly provided by Max Bopp. The other values are calculated as discussed in section 4. The data was recorded in June* 2015.

Wind[Hz]	Fetch [m]	Live	Statistics	Spectrum	pdf-Fit
10	2	0.001058	0.001057	0.0012798	0.0008313
	7	0.015982	0.016021	0.0176415	0.0131641
	12	0.024884	0.024498	0.0252318	0.0145159
	21	0.034927	0.034181	0.0341817	0.0286111
12.6	2	0.014595	0.0148495	0.0164016	0.015299
	5	0.028482	0.0281202	0.0287801	0.029784
	7	0.0345	0.0342125	0.0347234	0.030919
	9	0.039407	0.0390065	0.0391395	0.037332
	12	0.043849	0.0434649	0.0427277	0.038307
	21	0.039942	0.0392729	0.0383766	0.042535
15.8	1	0.012371	0.0122653	0.013941	0.00868
	3	0.045807	0.0457916	0.045021	0.03493
	5	0.047233	0.0467676	0.045737	0.04023
	7	0.051131	0.0511203	0.050153	not fittable
	12	0.056276	0.0562292	0.053934	0.04075
	21	0.050897	0.0505589	0.046855	not fittable
19.9	2	0.061619	0.0611376	0.059431	0.05343
	3	0.061452	0.0613008	0.059611	0.05207
	12	0.070981	0.0709184	0.066055	0.07701
	21	0.073321	0.0725685	0.065557	0.09621
25.1	1	0.079741	0.079451	0.076198	0.07571
	2	0.074192	0.073886	0.071819	0.07283
	3	0.08407	0.083456	0.077393	not fittable
	12	0.101358	0.100753	0.090112	0.07999
	21	0.103953	0.104513	0.092901	0.1423

Table 2: *Calculated values for σ_{mss} under fetch conditions. The values of the live-calculation are taken from the corresponding documentations of the measurement. The other values are calculated as discussed in section 4.*
The data was recorded in July 2015.

Erklärung

Ich versichere, dass ich diese Arbeit selbstständig verfasst und keine anderen als die angegebenen Quellen und Hilfsmittel benutzt habe.

Heidelberg, den 29. Juli 2016,